

Article

Seabed Mapping Using Shipboard Multibeam Acoustic Data for Assessing the Spatial Distribution of Ferromanganese Crusts on Seamounts in the Western Pacific

Jongmin Joo¹, Seung-Sep Kim², Jee Woong Choi³, Sang-Joon Pak¹, Youngtak Ko¹, Seung-Kyu Son¹, Jai-woon Moon¹ and Jonguk Kim^{1,*} 

¹ Deep-Sea Mineral Resources Research Center, Korea Institute of Ocean Science & Technology, Busan 49111, Korea; joojongmin@gmail.com (J.J.); electrum@kiost.ac.kr (S.-J.P.); ytko@kiost.ac.kr (Y.K.); skson@kiost.ac.kr (S.-K.S.); jwmoon@kiost.ac.kr (J.-w.M.)

² Department of Geological Sciences, Chungnam National University, Daejeon 34134, Korea; seungsep@cnu.ac.kr

³ Department of Marine Science & Convergence Engineering, Hanyang University ERICA, Gyeonggi-do 15588, Korea; choijw@hanyang.ac.kr

* Correspondence: jukim@kiost.ac.kr; Tel.: +82-51-664-3465

Received: 22 November 2019; Accepted: 5 February 2020; Published: 11 February 2020



Abstract: Cobalt-rich ferromanganese crusts (Fe–Mn crusts), potential economic resources for cobalt, nickel, platinum, and other rare metals, are distributed on the surface of seamounts, ridges, and plateaus. Distribution of Fe–Mn crust deposits and their geomorphological characteristics are prerequisites to selecting possible mining sites and to predicting the environmental impact of deep-sea mining activity. Here, we map the spatial distribution of Fe–Mn crust deposits on seamount summits and flanks in the Western Pacific using shipboard multibeam echo sounder (MBES) data and seafloor images from a deep-towed camera system (DCS) and evaluate the relationship between acoustic backscatter variations and the occurrence of Fe–Mn crusts. We find a positive correlation between high backscatter intensity, steep seabed slope gradients, and the occurrence of Fe–Mn crusts. However, our analysis was not effective to distinguish the spatial boundary between several seabed types that occur over small areas in mixed seabed zones, particularly where transition zones and discontinuous seabed types are present. Thus, we conclude that MBES data can be a valuable tool for constraining spatial distribution of Fe–Mn crust deposits over a large exploration area.

Keywords: ferromanganese crust; seamounts; shipboard multibeam survey; acoustic backscatter intensity; seafloor observation; seabed classification

1. Introduction

The seamounts in the Western Pacific are littered with ferromanganese (Fe–Mn) crusts, which are potential economic resources containing cobalt, nickel, platinum, and other rare metals [1–3]. Fe–Mn crusts from these seamounts are characterized by higher concentrations of rare metals originating from continental crust through weathering and submarine volcanism [1,2]. Thus, the Western Pacific has been considered as a prime zone for geological and geophysical exploration of Fe–Mn crusts by several countries [2]. As a result, four exploration licenses (Russia, China, Japan, and Korea) in the Western Pacific region were granted by the International Seabed Authority by 2018. In order to examine feasibility of mining Fe–Mn crusts, spatial distribution of Fe–Mn crust deposits and their geomorphological characteristics have to be constrained using sea-surface and near-bottom observations.

Marine scientists have long used highly sophisticated acoustic seabed-mapping systems to observe detailed morphological variations of the seabed and a wide variety of deep-sea environments [4–6]. Seabed-mapping sonars, such as multibeam and single-beam echo sounders, have generally been used for bathymetric and sediment property mapping. In particular, shipboard multibeam acoustic data have been used with high reliability in sustainable management of coastal marine systems, seabed resource assessments, and offshore engineering. Furthermore, multibeam echo sounder (MBES) installed on the underwater platforms, such as autonomous underwater vehicles (AUVs) or remotely operated vehicles (ROVs) operating near seafloor, can produce the most high-resolution (i.e., grid spacing < 1 m) seabed maps [6–8]. However, utilizing such near-bottom acoustic surveys is less recommended during the initial stage of exploration due to time and cost constraints. Therefore, it would be more effective to first understand the basic environmental parameters of the survey area, including morphology, surficial seabed sediment, and others, using shipboard MBES data, and then select target areas for detailed investigation with high-resolution mapping.

MBES bathymetry data provide spatial information on seabed relief, which can be used to infer geological and geomorphological characteristics of seafloor [9,10]. Furthermore, MBES backscatter data have been widely used to delineate benthic habitat patches for managing marine ecosystems and to classify the seafloor types for mapping distribution of seabed resources (e.g., manganese nodules) [5,6,11–17]. Acoustic intensities backscattered from the seabed usually require postprocessing to remove intensity variations that are unrelated to acoustic seabed properties, including propagation loss depending on sound-speed profiles in the operating area. System parameters such as the transmission (source) level, reception sensitivity, beam pattern, and signal duration, can also influence backscatter intensity. The processed bottom backscattering strength [18,19] generally varies depending on roughness of water–seabed interface and volume inhomogeneities in the sediment [20–33]. For example, the rougher the surface, the lesser energy will be reflected at the specular angle and the more energy will be scattered in the other directions [11]. Thus, coarse sediments typically exhibit high backscatter intensity owing to high bulk density, high acoustic impedance contrast, and large roughness of the sediment–water interface, whereas fine sediments result in low intensity because of low acoustic impedance contrast along the water–sediment interface [18,34–36]. Such variations in seabed backscatter intensity have been related with the presence of polymetallic Mn nodules and Fe–Mn crusts.

To enhance the detectability of seabed resources, there has been an effort to use both acoustic (ship-based MBES and deep-tow side-scan sonar data) and ground-truth data (underwater video data and core sampling) for inferring the distribution and abundance of Fe–Mn crusts. Usui and Okamoto [1] analyzed side-scan sonar images, seafloor observations, and dredge sampling to estimate the spatial distribution of Fe–Mn crusts and reported that the high acoustic backscatter on the flanks of seamounts is associated with Fe–Mn crusts covered in hard substrate. Thornton et al. [8] proposed that 3-D color reconstructions of the seabed generated from acoustic sensor, laser, and a light-emitting diode (LED) array data can be used to accurately estimate the volumetric distribution of Fe–Mn crusts. Joo et al. [37] recently argued that a positive correlation between shipboard MBES backscatter variations and the occurrence of Fe–Mn crusts can be utilized for characterizing spatial distribution of Fe–Mn crusts covering the outer rim of summit and slopes of seamounts.

Here, we characterize the spatial distribution of Fe–Mn crusts from the Magellan Seamounts in the Western Pacific using shipboard MBES and deep-towed camera system (DCS) data. We focus our analyses on the periphery of the seamount summit areas, where Fe–Mn crusts may occur irregularly at the transition zone between the sedimentary cap and substrate rock [37]. We first make qualitative and quantitative interpretations of the MBES data, with a particular focus on the geometric and geological characteristics of the seabed that may influence the acoustic backscatter variations. We then evaluate relationships between the acoustic backscatter variations and the occurrence of Fe–Mn crusts based on the shipboard MBES and DCS data. This study demonstrates that our approach can be applied to

classify seabed types hosting Fe–Mn crust deposits and predict the spatial distribution of Fe–Mn crust deposits for both a single seamount and all of the seamounts in a given survey area.

2. Materials and Methods

2.1. MBES Data Acquisition and Processing

We acquired MBES data and seafloor observations at 13 seamounts in the Western Pacific using the R/V Onnuri of the Korea Institute of Ocean Science and Technology (KIOST) (Busan, Korea) during 2013–2015 (Figure 1). Multibeam data were obtained from a hull-mounted 12 kHz Kongsberg Simrad EM120 multibeam sonar system (Kongsberg Maritime, Kongsberg, Norway), fully compensated with the vessel position and motion (heave, pitch, roll, and yaw). Here, vessel positioning was determined by a differential global positioning system (DGPS). The EM120 system has 191 beams with pointing angles that are automatically adjusted based on the achievable coverage or operator-defined limits. It has a swath width of 120°, with along- and across-track beam sizes of 1° and 2°, respectively. The MBES survey lines were primarily oriented along NE–SW tracks, with an approximately 7-km line spacing, which provided at least 30% overlap (Figure 1b). The sound speed profiles in the water column were collected before starting the MBES survey at each seamount. The size of the beam footprint, which is a function of the MBES operating depth, varied from 52 to 157 m in the along-track direction for a beam with a 60° incidence angle as the bathymetry across the study area was in the 1300–5500 m range. Kongsberg Simrad SIS (Seafloor Information System) software (version 4.3.0, Kongsberg Maritime, Kongsberg, Norway) was used for positioning and logging MBES data.

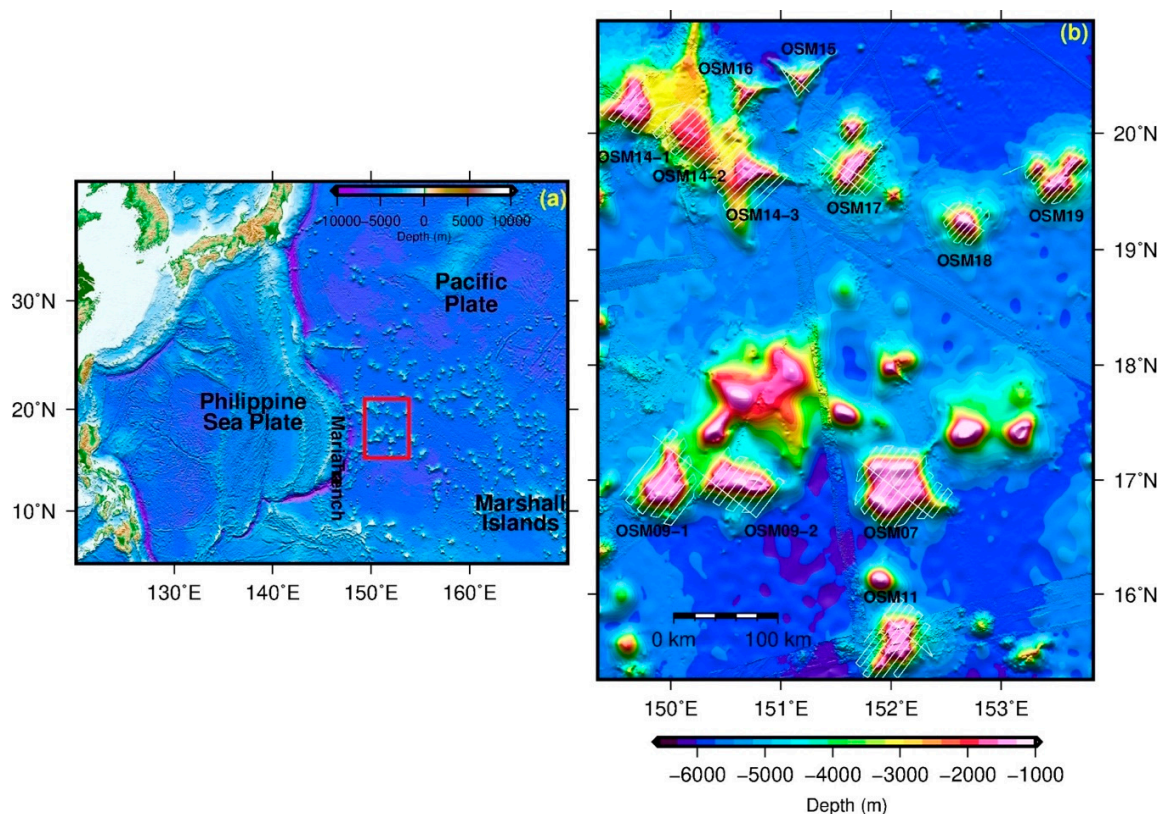


Figure 1. (a) Regional bathymetry map of the study site in the Western Pacific. The study area is denoted as the red box; (b) bathymetric map of the study area showing a compilation of Simrad multibeam data of R/V Onnuri and predicted data from Ryan et al. [38]. White dashed lines are the ship tracks of R/V Onnuri.

Postprocessing on the multibeam bathymetric data was performed using the MB-System's software (version 5.7.5, MBARI, CA, USA), involving removal of navigation errors, noise reduction, removal of poor-quality beams, and sound speed corrections [39]. The processed data were spatially reorganized into a regular matrix (a grid or a Digital Terrain Model) via the kriging interpolation method. The final processed bathymetric grids were resampled to a uniform grid at a 100 m gridding spacing using Generic Mapping Tools software [40].

The EM120 system also collected backscatter data, which contain important information on seafloor morphology and physical properties. Backscatter data are inherently noisy and require extensive processing to remove artifacts caused by recording equipment, seafloor topography, and water column properties [41–44]. The backscatter data were processed using the Fledermaus Geocoder Toolbox (FMGT) software (version 7.6.2, QPS BV, Zeist, The Netherlands), which provides functionalities for radiometric corrections (removal of acquisition gains, power levels, pulse widths, insonification areas, and incidence angles), geometric corrections (compensation of slant-range distortion and navigation errors), antialiasing, and speckle removal algorithms [45]. As a final product, FMGT yields the relative intensity of the backscatter signal that does not depend on the beam's grazing angle in the output data. However, false high-backscatter stripes were still present in the postprocessed data due to incomplete nadir corrections and/or other noise. The final postprocessed backscatter data were gridded to produce backscatter grids of 100 m resolution.

A comparison of the backscatter datasets obtained at the different seamounts was straightforward because the same hardware, software, and acquisition system and calibration parameters were applied during each of the MBES surveys (2013–2015).

2.2. Seafloor Observation Using Camera Tow

In situ visual observations were performed using a DCS from the KIOST) to record seabed images. Thirty-four camera tow lines were collected at 12 seamounts (black lines in Figure 2). These tow lines were selected based on the variations in the observed MBES backscatter intensity. Seafloor observations were made primarily on the summit areas and upper flanks of the seamounts (1300–2500 m water depths). The main purposes of the camera observations were to inspect the seabed types and visually confirm the occurrence of Fe–Mn crusts. The DCS was towed 5–15 m above the seabed at 0.5–1.5 knots. Two parallel lasers mounted on the DSC were used to estimate the size of the nearest materials and mark the transect width in the recorded video. The high-resolution digital video footage consisted of 15 s sequences that were analyzed following the method described in Usui and Okamoto [1] to identify local-scale sediments and seabed morphology types. Our qualitative assessment of the surficial seabed sediments was based solely on the color and texture of the seafloor recognized from the video footage as no systematic direct sampling of the sediments was conducted.

We used the DSC data to categorize the sedimentary substrate types based on the presence of Fe–Mn crust deposits as follows: a “crust-dominant floor”—the seabed video footage included >90% Fe–Mn crust deposits; a “sediment-dominant floor”—the video footage included >90% sediments; and “combined sediment types”—the video footage included several sediment types (i.e., Fe–Mn crusts, nodules, unconsolidated sediments, and ripple marks).

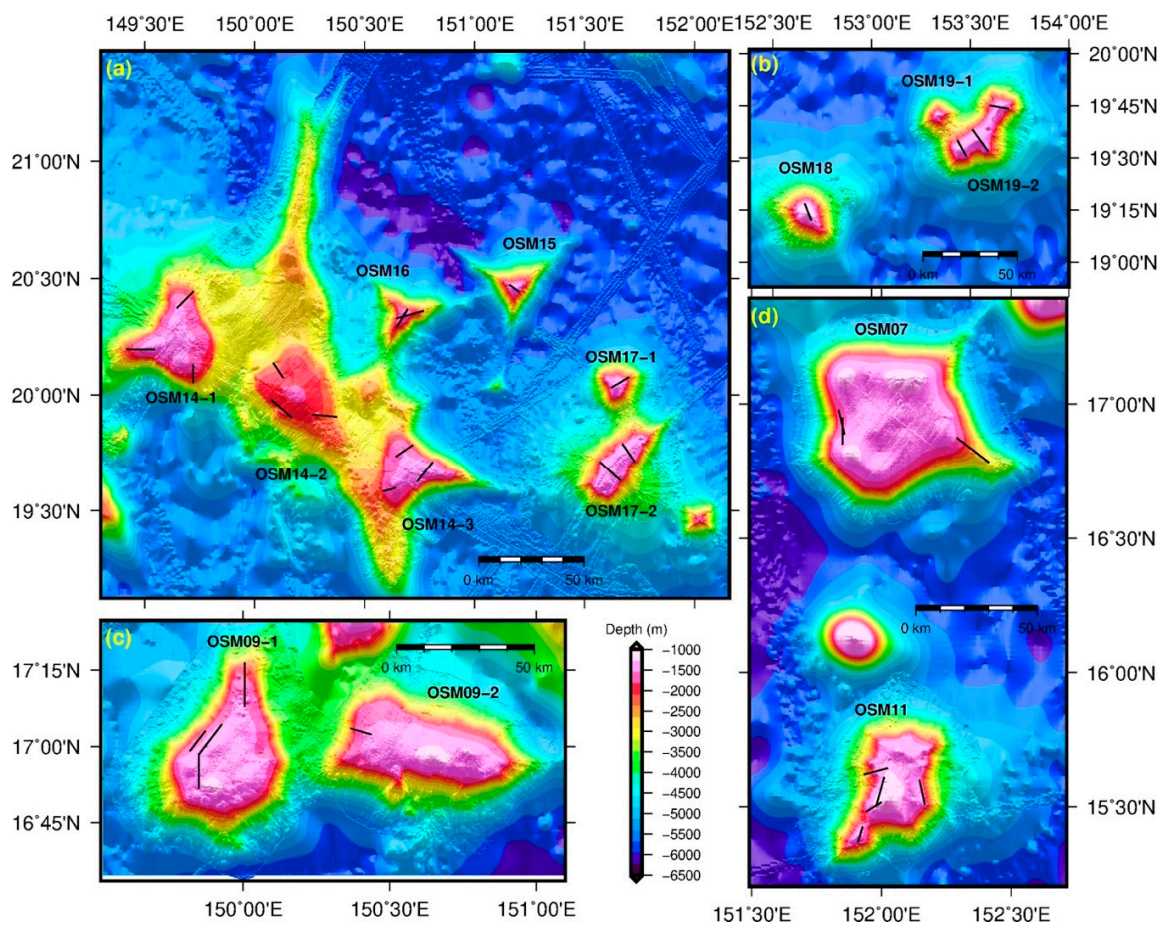


Figure 2. Multibeam-derived bathymetry shadow-relief maps of seamounts in the (a) northwest (OSM 14, OSM 15, OSM 16, and OSM 17), (b) northeast (OSM 18 and OSM 19), (c) southwest (OSM 9), and (d) south sectors (OSM 7 and OSM 11) of Figure 1b. Black lines are the transects of the deep-sea camera system (DCS) survey locations.

3. Results

3.1. Seafloor Morphology

Most seamounts in our study area exhibited a depth range from 1500 m at the summit to 6000 m at the base of the slope (Figure 2). Based on the size of summit area (i.e., showing slopes $<5^\circ$), we categorized the 13 seamounts into Type 1 (OSM 7, OSM 9, OSM 11, and OSM 14) and Type 2 (OSM 15, OSM 16, OSM 17, OSM 18, and OSM 19) seamounts. Type 1 seamounts exhibit a flat summit occupying a large portion of the mapped area ($>500 \text{ km}^2$) (Figure 2a,c,d). OSM 14 with three triangular-shaped guyots appears to be the largest flat seamount in the study area (Figure 2a). OSM 9-1, OSM 14-1, and OSM 14-2 have relatively flat summits with many small cone-shaped volcanoes ($<50 \text{ m}$ in diameter) (Figure 2a,c), whereas OSM 7 has a terrace in the southeast direction (Figure 2d). Conversely, Type 2 seamounts are characterized by conical shapes and narrow flat-top surface areas ($<500 \text{ km}^2$) (Figure 2a,b). Type 2 seamounts are generally smaller than Type 1 seamounts. OSM 15 and OSM 16 exhibit tetrahedron shape in planar view, while OSM 17-1, OSM 18, and OSM 19-1 show nearly conical shape. OSM 17-2 and OSM 19-2, however, have NE–SW-elongated flat summits (Figure 2a,b).

We computed the slope gradients from the observed MBES bathymetry (Figure 3). Slope gradients of the seamount summits range between 2.5° and 7.5° , whereas the seamount flanks exhibit steep slopes of 10° to $>20^\circ$ (Figure 3). There is a distinct break of slopes at ~ 1600 m depth, which marks the flat-summit margin of Type 1 seamounts (OSM 7, OSM9, OSM11, OSM 14-1, and OSM 14-3), with an exception of OSM 14-2 (Figures 2 and 3). There is a marked increase in slope gradient from a mean gradient of $\sim 5^\circ$ to $\sim 25^\circ$ below this depth. The seabed adjacent the seamounts is relatively flat with slopes less than 5° .

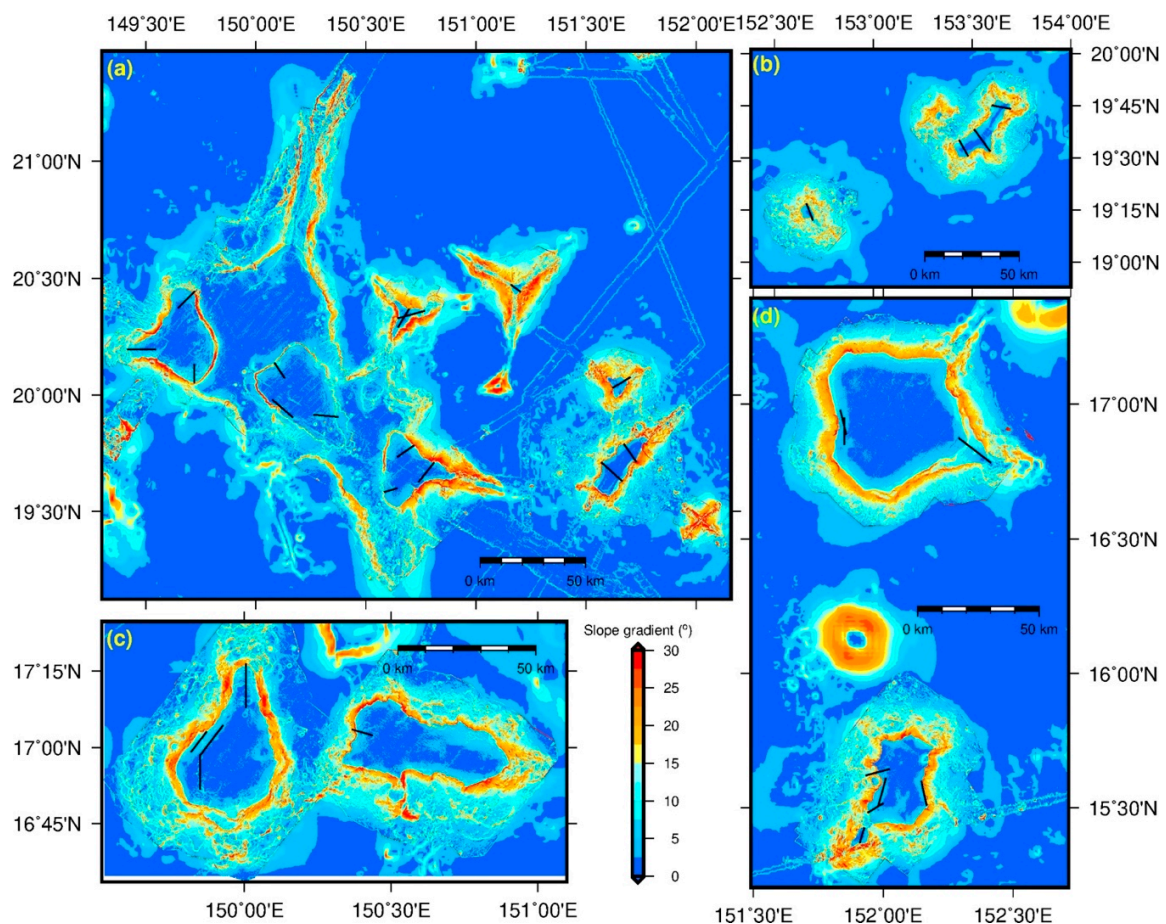


Figure 3. Multibeam-derived slope gradient maps of seamounts in the (a) northwest, (b) northeast, (c) southwest, and (d) south sectors of Figure 1b. Black lines are the transects of the DCS survey.

3.2. Seabed Backscatter Intensity

The acoustic backscatter data provide additional information on seafloor morphologies and substrates (Figure 4) because relative backscatter intensity can be correlated with seabed roughness and hardness. Backscatter intensity values of the seamounts range between -50 and -10 dB (Figures 4 and 5). Type 1 seamounts span a broader range of backscatter intensity than Type 2 seamounts. Type 1 seamounts (OSM 7, 9, 11, and 14) exhibit a bimodal distribution of backscatter intensity values with two modal peaks located between -45 and -15 dB (Figure 4a,c,d and Figure 5). Considering that most surface areas of Type 1 seamounts are the flat summits having low backscatter values of -45 to -35 dB, such bimodal distribution can be useful to classify summit and slope regions in the backscatter intensity data (yellow lines in Figure 4). Conversely, Type 2 seamounts (OSM 15, 16, 17, 18, and 19) exhibit a typical single-peak histogram of backscatter intensity values located between -35 and -10 dB, which cannot be used for further classification (Figure 4a,b and Figure 5a).

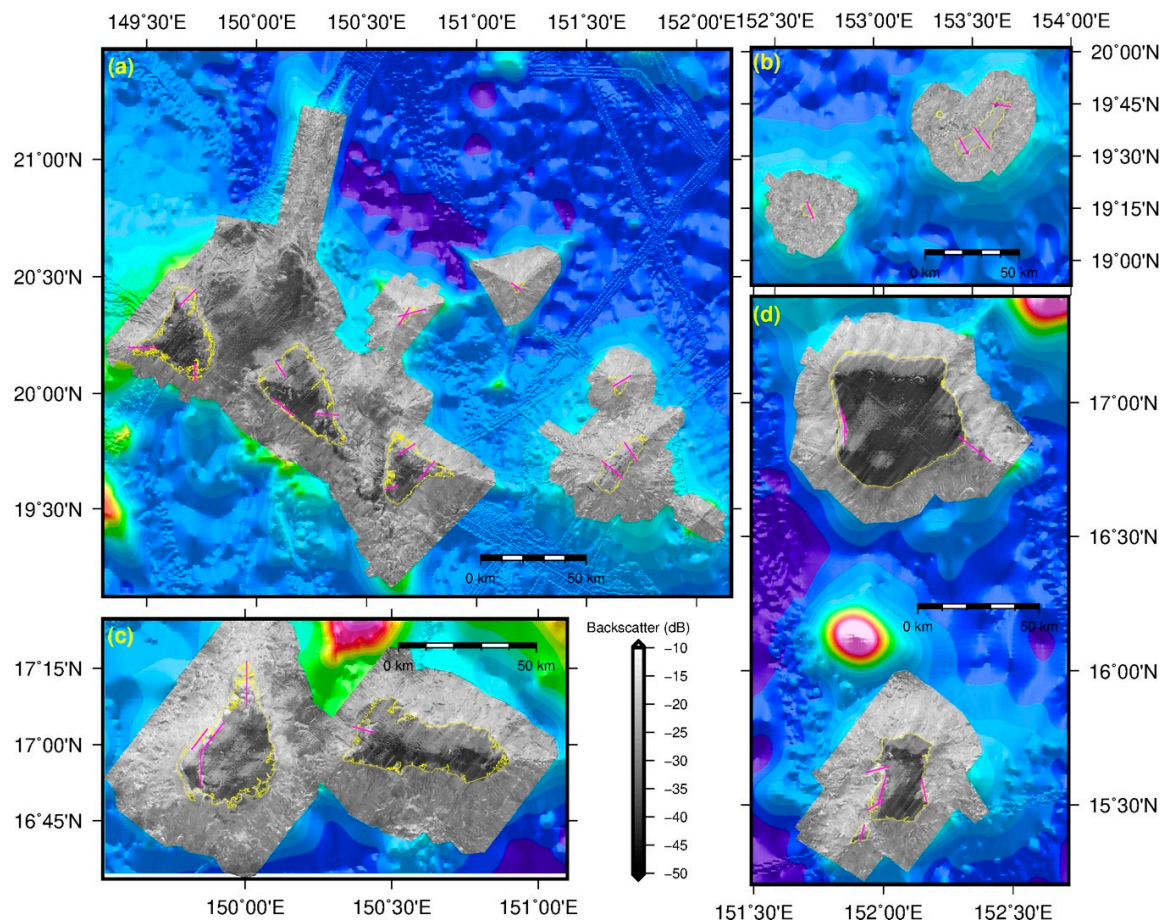


Figure 4. Multibeam-derived backscatter maps overlaid with a hillshade bathymetry of seamounts in the (a) northwest, (b) northeast, (c) southwest, and (d) south sectors of Figure 1b. Magenta lines are the transects of the DCS survey, and yellow dashed contours indicate summit areas with a gradient of $<5^\circ$.

3.3. Seafloor Video Characterizations

We utilized the seafloor video footage acquired at the summit area and upper flanks of target seamounts to verify whether the observed variations of acoustic backscatter in the MBES data were inherently correlated with the actual seabed conditions. First, we classified the seafloor in the study area into five types based on photographs taken along the DCS transects (see magenta lines in Figure 4): (1) crust-dominant floor (C1 type), (2) crust partially covered by sediments (C2 type), (3) crust covered by sediments with ripple marks (C3 type), (4) sediments covered by nodules (N type), and (5) sediments-dominant floor (S type) (Figure 6). Fe–Mn crusts were identified on the flanks of Type 1 seamounts and along the edges of the summit areas (OSM 7, 9, 11, and 14), which might modulate the observed acoustic backscatter intensities (Figure 7). Apart from the outer rim to the center of the summit (A–A' and C–C' tracks in Figure 7b), the coverage of Fe–Mn crusts on the seabed tends to decrease. Hard substrata with mixed habitats of volcanic outcrops and Fe–Mn crusts are juxtaposed with homogeneous soft sediments that contain ripples and sandwaves (Figure 6b,c) in the transitional areas between the outer rim and the center on the summit of seamounts (B–B' tracks in Figure 7a,b). Our results demonstrate that occurrence of Fe–Mn crusts is limited to a few rocky outcrops and rocky walls in the soft sediment-dominated areas (near A' and C' locations in Figure 7b).

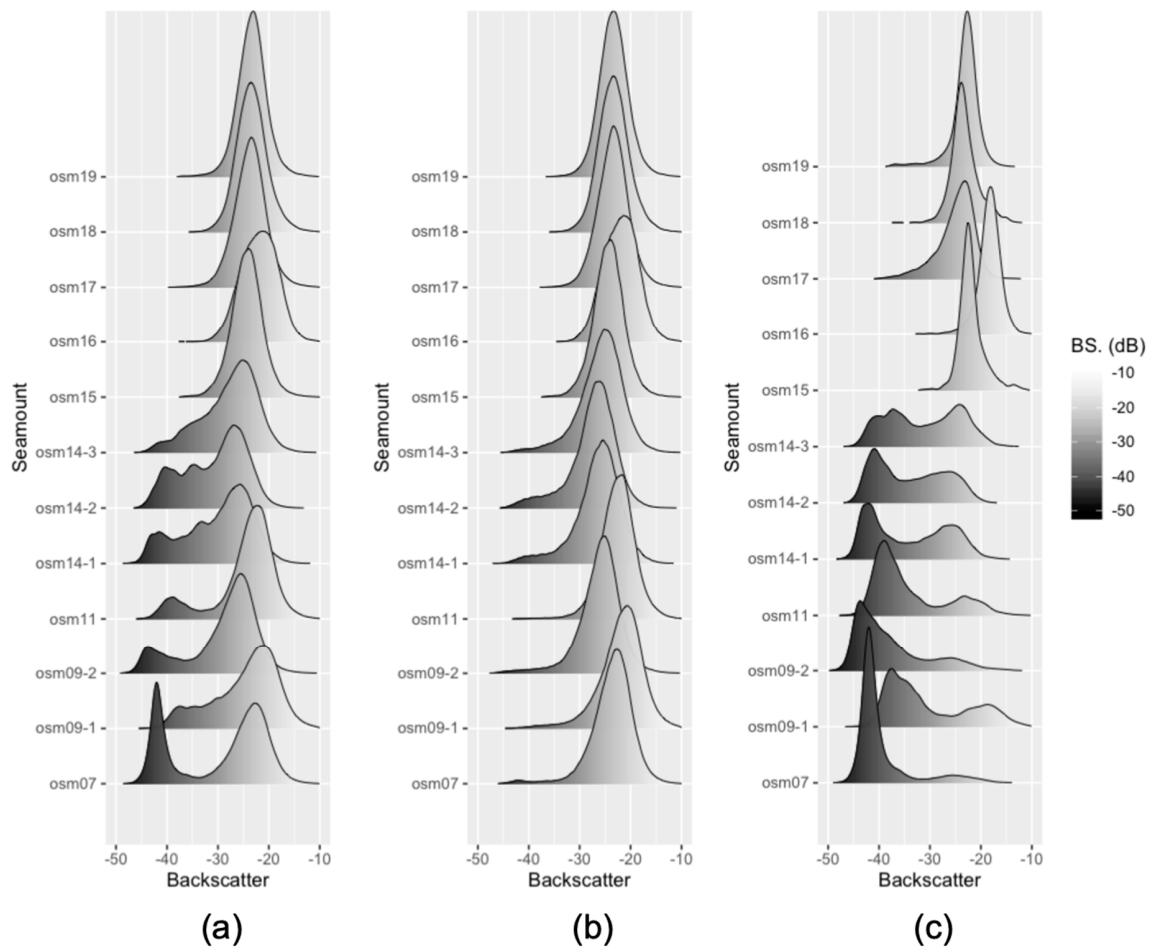


Figure 5. Multiple histograms of multibeam echo sounder (MBES) backscatter data extracted by the distinguished areas associated with (a) whole seamount, (b) flank area only, and (c) summit area only of target’s seamounts.

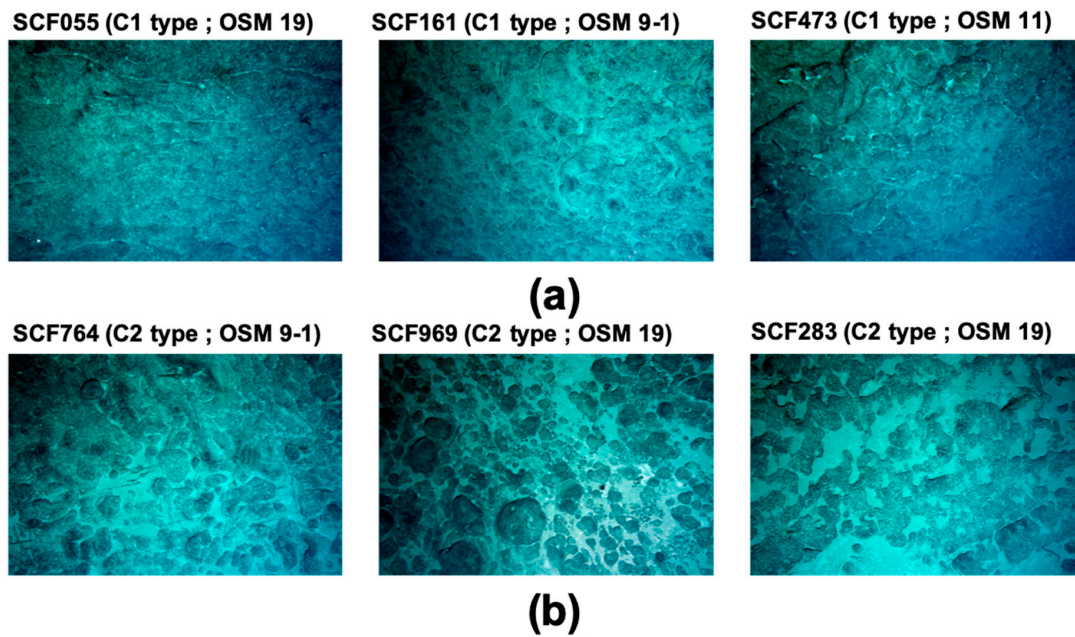


Figure 6. Cont.

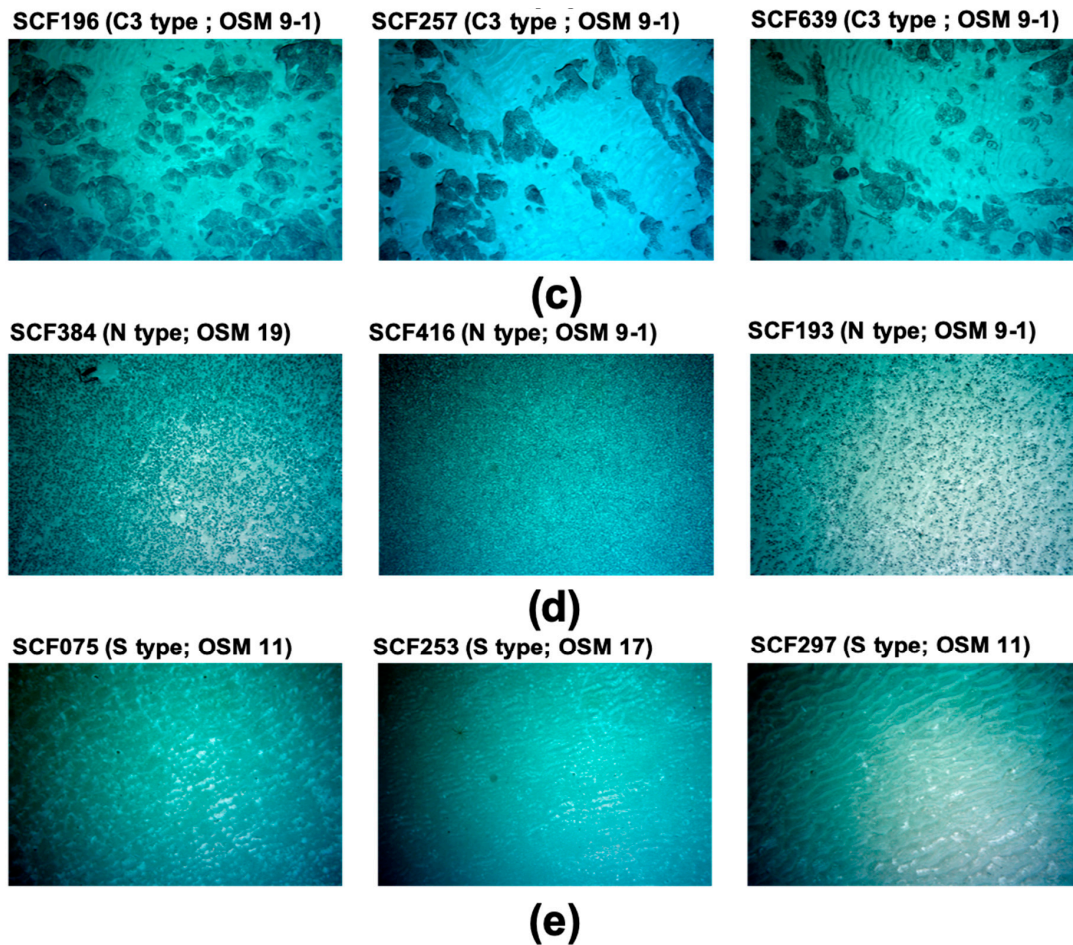


Figure 6. Examples of seabed types observed from the DCS: (a) crust-dominant floor (C1 type), (b) crust partially covered by sediments (C2 type), (c) crust covered by sediments with ripple marks (C3 type), (d) sediments covered by nodules (N type), and (e) sediments-dominant floor (S type).

However, crust-covered bedrock with sediments is predominant in the center and edges of Type 2 seamount summits (OSM 15, 16, 17, 18, and 19) (Figure 8). S-type seabed is characterized by little population at OSM 16 and 18 (Figure 8a,b). Mixed seafloor types (C2 and C3) are the predominant substrates at the OSM 17 and 19 (Figure 8c,d). Consolidated sediments with polymetallic nodules are also observed at the boundary between two different seafloor types characterized at OSM 17 (tracks A–A' and B–B' in Figure 8c).

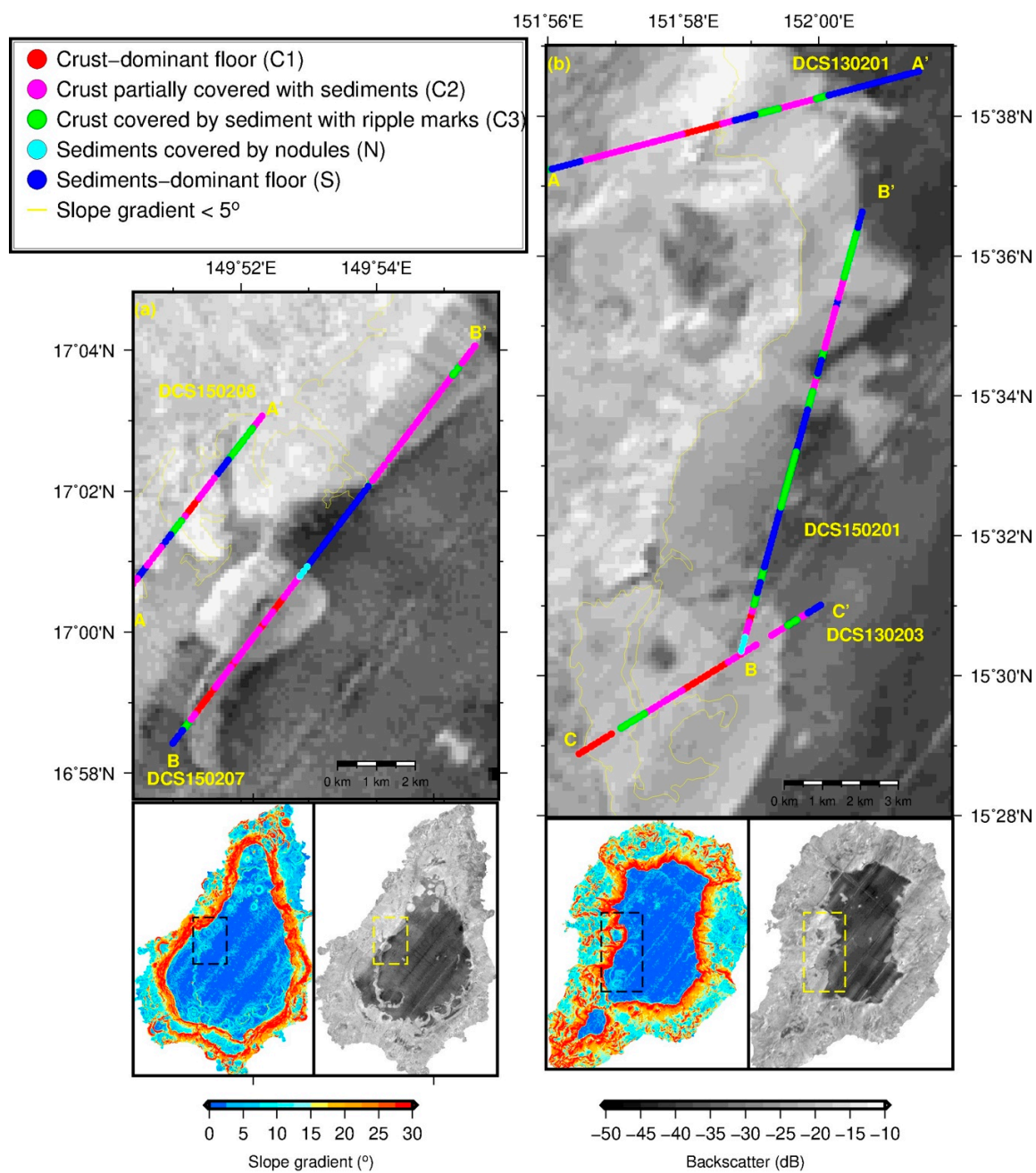


Figure 7. MBES backscatter maps showing distribution of the seabed types within the upper flanks and summit in Type 1 seamounts: the enlarged areas of (a) OSM 9-1 and (b) OSM 7. Yellow dashed contours indicate summit areas with gradients of $< 5^\circ$. The two lower panels show slope gradient (left) and acoustic backscatter (right) maps, corresponding to OSM 9-1 and OSM 7, respectively.

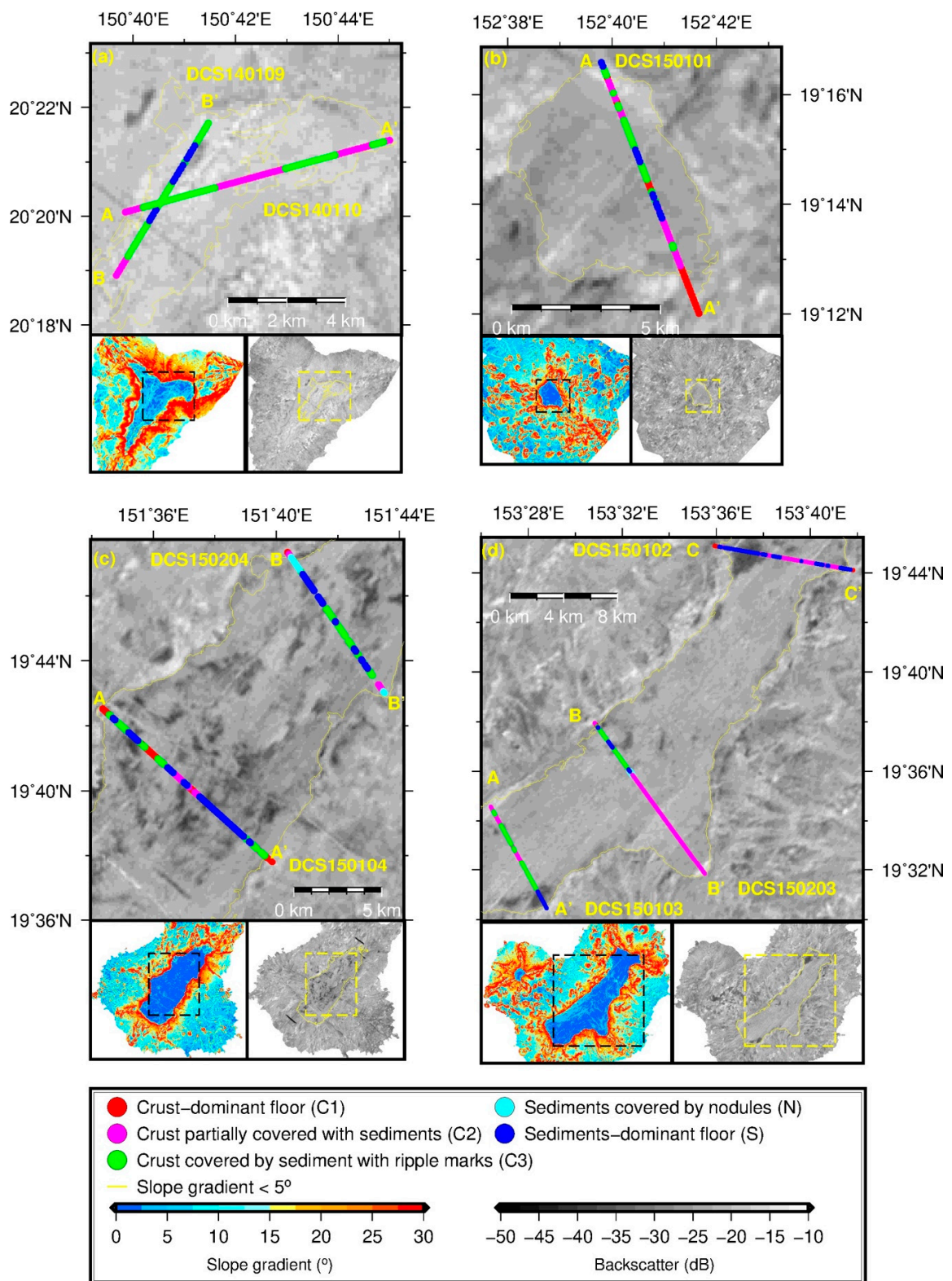


Figure 8. Expanded MBES backscatter map showing distribution of the seabed types within the summit in Type 2's seamounts observed from DCS surveys: the local area of (a) OSM 16, (b) OSM 18, (c) OSM 17, and (d) OSM 19. Yellow dashed contours indicate summit areas with a gradient of $<5^\circ$. The two panels below the expanded map (Figure 8a–d) show information of (a) slope gradient and (b) acoustic backscatter, corresponding to the flanks and summit of target's seamounts.

3.4. Comparison between MBES Backscatter and Video Footage

The DCS and MBES data exhibit a positive correlation between the backscatter intensities, steep seabed slopes, and occurrence of Fe–Mn crusts [37]. However, this correlation is insufficient to delineate boundaries between several seabed types occurring over small areas. The box-and-whisker plots in Figure 9 illustrate the differences in relative acoustic backscatter intensity for the DCS-surveyed seamounts. A comparison of the MBES backscatter intensities and seabed types for Type 1 seamounts (OSM 7, 9, 11, and 14) shows that the S-type seabed dominates the zones with MBES backscatter intensity values below -30 dB, whereas C2- or C3-type seabeds are dominant, showing backscatter intensity values above -30 dB (Figure 9a). For example, three DCS transects located in the outer rim of OSM 9-1 and OSM 11 (two tracks in Figure 7a and B–B' track in Figure 7b) were classified as C2-/C3-type seabeds with intermediate backscatter intensity values (approximately -30 to -20 dB). In these areas, Fe–Mn crusts and consolidated sediments were observed in the video footage (Figure 9a).

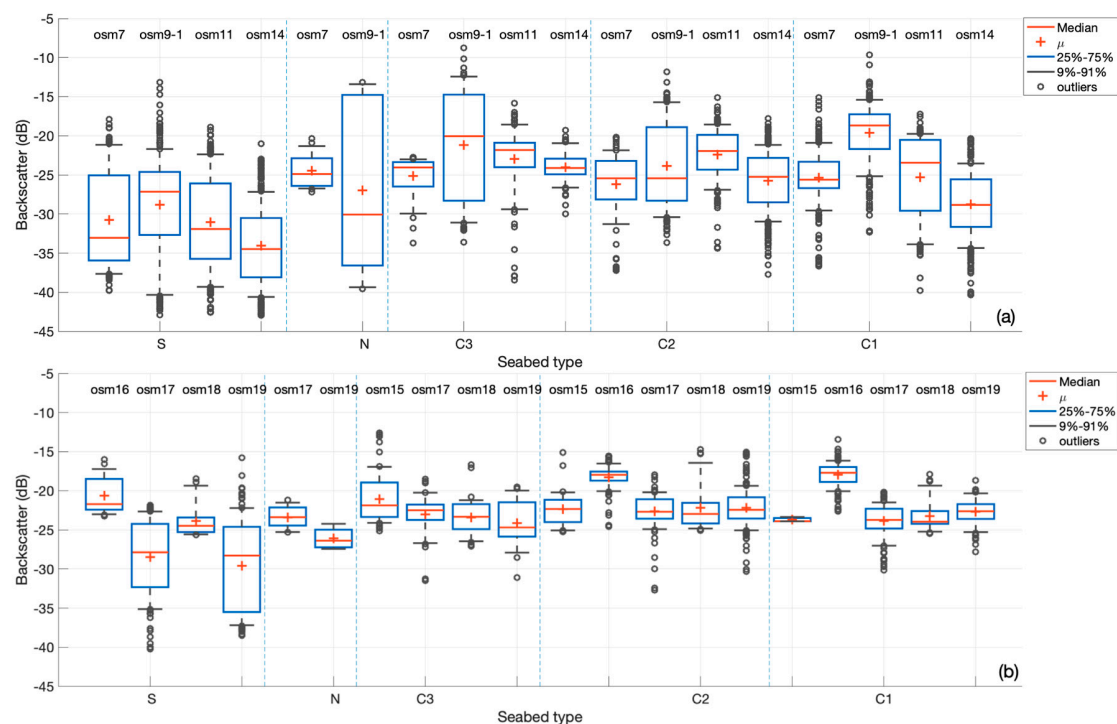


Figure 9. Box-and-whisker diagrams showing relative backscatter intensity for each seabed type in the surveyed seamounts using acoustic data and optical results: (a) Type 1 seamounts (OSM 7, 9, 11, and 14), (b) Type 2 seamounts (OSM 15, 16, 17, 18, and 19). Box-and-whisker plot shows the median (bar), mean (plus), and interquartile (25–75%) range and outliers (circle) being 1.5 times this range.

An additional statistical analysis (density plot) of the MBES backscatter intensities was carried out to clarify the differences between Type 1 and Type 2 seamounts (Figure 10). Density plots of backscatter intensity versus slope gradient illustrate the entire shipboard multibeam dataset across the Type 1 and Type 2 seamounts (Figure 10a,c), whereas density plots of backscatter intensity versus depth are shown in Figure 10b,d. The corresponding seabed types observed along the DCS transects are overlaid onto the density plots for comparison. These density plots indicate that the number of gridded dataset (Figure 10a,b) in Type 1 seamount is two times greater than that in Type 2 (Figure 10c,d) due to the surface area difference between Type 1 and Type 2 seamounts. The density plots of Type 1 seamounts reveal that backscatter intensity values below -30 dB area associated with flat slope gradients ($<5^\circ$) and shallow water depths (<2000 m) (Figure 10a,b). Furthermore, the S-type seabed is largely present at Type 1 seamounts, where the backscatter intensity values are between -45 and -25 dB (Figure 10a) and over 2000 m in water depth (Figure 10b). Conversely, the density plots of Type 2 seamounts reveal

that backscatter intensity values between -30 and -15 dB are distributed along slope gradients of $<20^\circ$ and in both shallow (1300–1600 m) and deep areas (3500–4800 m) (Figure 10c,d). The S-type seabed is largely present at Type 2 seamounts where the backscatter intensity values are between -35 and -15 dB. This coincides with slope gradients of $<5^\circ$ and >1500 m water depth. As shown in Figures 9 and 10, the distribution (Figure 5) of backscatter intensities for Type 1 seamount is broader than that for Type 2 because the backscatter intensities at flat slope areas (gradients $<5^\circ$) is relatively lower than those in other areas.

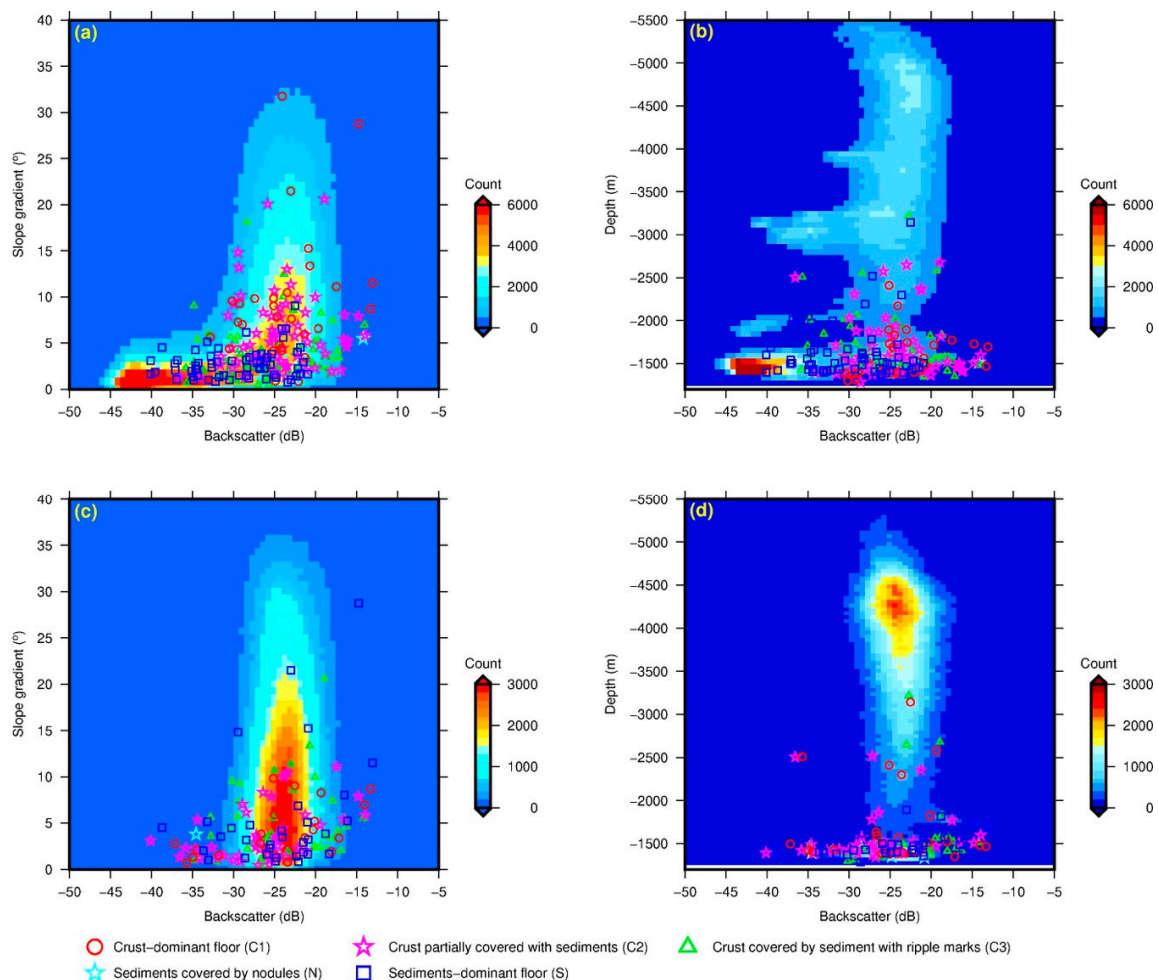


Figure 10. Density plots of backscatter versus slope gradients illustrate the shipboard MBES data of (a) Type 1's seamounts and (c) Type 2's seamounts. Other density plots of backscatter versus depth show the distribution of MBES data of (b) Type 1's seamounts and (d) Type 2's seamounts. Overlaid on density plots are the observed seafloor types extracted from DCS tracks corresponding to the seabed characterizations.

4. Discussion

4.1. Factors Affecting MBES Backscatter

The shipboard multibeam backscatter data give us particular information about the substrate that cannot be obtained by bathymetric data alone. At frequencies used by seafloor mapping sonars (tens to hundreds of kHz), the backscatter from the seabed is generally affected by two factors: (1) the interface roughness (e.g., seabed substrate, microtopography, etc.) and (2) volume heterogeneity (e.g., sediment grain size, bioturbation, and changes of sediment acoustic parameters) [14,46,47]. The contribution of both factors to the total scattering depends on the hardness (i.e., acoustic impedance). It is assumed

here that the microscale roughness due to cobalt-rich Fe–Mn crusts is too small to discriminate using a 12 kHz MBES because the bathymetric resolution (a few tens of meters) of the MBES at 1500–5000 m water depths is insufficient to distinguish the roughness difference between areas with and without cobalt-rich Fe–Mn crusts. Therefore, the observed variations in the 12 kHz MBES backscatter data can be attributed to local heterogeneities in the surficial seabed properties. It is necessary to consider the primary features related to the spatial variations in acoustic backscatter during the interpretation of MBES backscatter data acquired on the surveyed seamounts.

The flanks of the surveyed seamounts correspond to areas with relatively high backscatter intensity and steep slopes, with gradients of $>15^\circ$ (Figure 3, Figure 4, and Figure 5b). It is well known that the flanks of the seamounts, which generally consist of a sediment-free hard rock substrate, is an important factor influencing high acoustic backscatter [1,33,37,46,48]. Thus, the single peak distribution of the backscatter intensity patterns owing to high backscatter on steep slopes ($>15^\circ$) suggests a hard seafloor and seabed relief are the principal factors influencing these high backscatter intensities (Figure 5b).

The summits of Type 1 seamounts show different properties between their outer rims and centers (Figure 3, Figure 4, and Figure 5c). The summit rims generally possess intermediate backscatter intensity values (approximately -30 to -20 dB), whereas the summit centers possess low backscatter intensity values between -45 and -30 dB (Figures 4 and 5c). The seabed relief may not be a responsible factor for the observed fluctuation of backscatter intensity, as slope gradients of the summits area of Type 1 seamounts are less than about 5° . Therefore, the spatial variability of seabed sediment properties is a plausible factor influencing the variation of MBES backscatter [33,37,46]. However, the summits of Type 2 seamounts possess relatively uniform, high backscatter intensity values (approximately -30 to -15 dB) (Figures 4 and 5c). The acoustic pattern observed in Type 2 seamounts is consistent with the results of Usui and Okamoto [1], which demonstrated that the high acoustic backscatter zones within conical-shape seamount were well related to limestone outcrop and substrates covered with ferromanganese crusts.

4.2. Relationship between MBES Backscatter and Occurrence of Fe–Mn Crusts

We compared the occurrence of Fe–Mn crusts with MBES backscatter intensity along all of the DCS transects to delineate their relationship (Figures 7–9). In order to ascertain the status of boundary zones distinguished by the backscatter data, the DCS tracks on Type 1 seamounts were chosen to traverse zones of different backscatter intensity values from upper flanks to the sedimentary cap on the seamount summits (Figure 4a,c,d). C1- and C2-type seabeds dominated the upper flanks (Figure 7) and were associated with higher backscatter intensity values (above approximately -30 dB; Figure 9a). The S-type seabed, which was frequently observed near the center of the summits, was associated with lower backscatter intensity values (below -30 dB) (Figures 7 and 9a). These findings are consistent with the results of Hein [2], which suggest that Fe–Mn crusts form only where the hard substrate is sediment-free. However, no dominant seabed type was observed in the outer rim of summits, which possessed an intermediate range of backscatter intensity (-30 to -20 dB) (Figures 7 and 9a). Although the sections with backscatter intensity values below -30 dB were highly correlated with S-type seabed areas in the outer rim (B–B' track lines in Figure 7a,b), other seabed types (types C2, C3, and N) were difficult to discriminate owing to the similar range of acoustic backscatter intensity associated with each seabed type. These results may be relevant to the resolution characteristics of MBES data, as the signal resolution (a few tens of meters) acquired 12 kHz multibeam sonar, which is insufficient to identify mixed substrata (at a scale of a few decimeters to a few decameters) on the outer rim of the summit [33]. Finer sediments (e.g., silt, sandy silt) generally exhibit a higher sensitivity to different acoustic frequencies (~ 10 – 85 kHz) than coarser sediments (e.g., gravel, shells, or sedimentary rocks) [20,49], such that seafloor roughness and sediment volume heterogeneity need to be considered when interpreting acoustic backscatter data in that frequency range [47,50]. These results indicate that the MBES spatial resolution of the 12 kHz multibeam backscatter data was sufficient to estimate the spatial distribution of Fe–Mn crusts, even though it was insufficient to discriminate the seafloor types

from mixed seabed features consisting of hard outcrops and soft sediments. Therefore, we infer that the two separated peaks distribution of acoustic backscatter that corresponds to the seamount summits is likely controlled by heterogeneities in surficial seabed properties rather than by seafloor geometry (Figure 5c), and postulate that MBES backscatter intensity across the summits of Type 1 seamounts reflects the occurrence of Fe–Mn crusts.

DSC transects were chosen to cross the entire summit areas of Type 2 seamounts to identify the sedimentary substrates corresponding to the single-peak-distributed backscatter patterns (Figure 4a,b and Figure 5c). C2- and C3-type seabeds dominate the seamount summits and are associated with higher backscatter values (above approximately -25 dB) (Figures 8 and 9b). The S-type seabed is not the dominant seabed type in the center of the flat summits (Figure 8). These summit areas are associated with an intermediate range of backscatter intensities (-30 dB to -20 dB), with the exception of OSM 17 and 19 (Figure 9b). These results suggest that an S-type seabed is either rarely present across the summits of Type 2 seamounts or concentrated only within small areas, as the acoustic footprint is not large enough to discriminate the various sedimentary environments. This occurs because the acoustic footprint of the ship-based multibeam sonar is much larger than the optical footprint of the near-bottom DCS, which can observe only small-scale areas in this deep-water environment. Backscatter intensity reflected from these DCS-scale areas, which are smaller than the size of sonar footprint and adjacent to other seabed types, may lead to an overestimation of the acoustic backscatter of these small-scale transitional and/or discontinuous seabed zones [33,46]. We conclude that the existence of Fe–Mn crusts around sediment-dominated areas on the summits of the surveyed seamounts is a major factor influencing the bimodal distribution of acoustic backscatter intensity values, with the exception of OSM 15, 16, and 18. Furthermore, the variations above the minimum intermediate backscatter intensity (i.e., above -30 dB) primarily indicate seabed hardness variations reflecting the occurrence of substrates covered with Fe–Mn crusts.

Our results suggest that ship-based multibeam backscatter data may be a valuable tool for constraining spatial distribution of Fe–Mn crust deposits during the early stage of mineral exploration. We combined acoustic backscatter, multibeam bathymetric, and seafloor observation data over a large exploration area ($10,150$ km²) to map the spatial distribution of Fe–Mn crust occurrence along seamount summits and upper flanks (Figure 11) using the parameters presented in Table 1. This classification map may provide useful spatial information to precisely estimate the distribution of Fe–Mn crusts. The mapping accuracy was tested using reference data from an underwater video dataset (Table 2). Potential Fe–Mn crusts (i.e., C1-, C2-, C3-, and N-type seabeds) were classified more accurately than the S-type seabed conditions.

An investigation of the spatial distribution of Fe–Mn crusts using relatively low-frequency multibeam sonar data (12 kHz) is limited in discriminating some mixed seabed types (i.e., heterogeneous soft-sediments and hard-outcrop areas) that may possess varying coverage of the Fe–Mn crust. For example, backscatter intensity associated with C1-, C2-, and C3-type seabeds exhibits no significant difference, although each seabed type is distinguishable in the DCS observations (Figure 9). Therefore, high-resolution seabed mapping (>30 kHz sonar system) via an AUV, ROV, or deep-tow side-scan sonar (DTSSS) is required to distinguish the detailed boundary conditions between different seabed types across the summits and slopes of the target seamounts [4,5,51]. The application of a broadband MBES system that can produce multispectral backscatter data may provide further details on the various seabed types, including the spatial coverage of Fe–Mn crusts [52–54].

Our joint analysis of the acoustic and DCS data confirmed that the summits of Type 1 seamounts were not only covered with unconsolidated sediments but also well-developed Fe–Mn crusts around the outer rims of the summits. The seabed surface area across the summits of Type 2 seamounts maintained a sediment-free environment, which enhances the potential for the growth of Fe–Mn crusts, even though the narrow summits of Type 2 seamounts possess relatively flat areas. These preliminary analyses suggest that a shipboard multibeam survey is a potentially effective approach for conducting an initial seabed resource assessment to ascertain the existence and general distribution of Fe–Mn crusts.

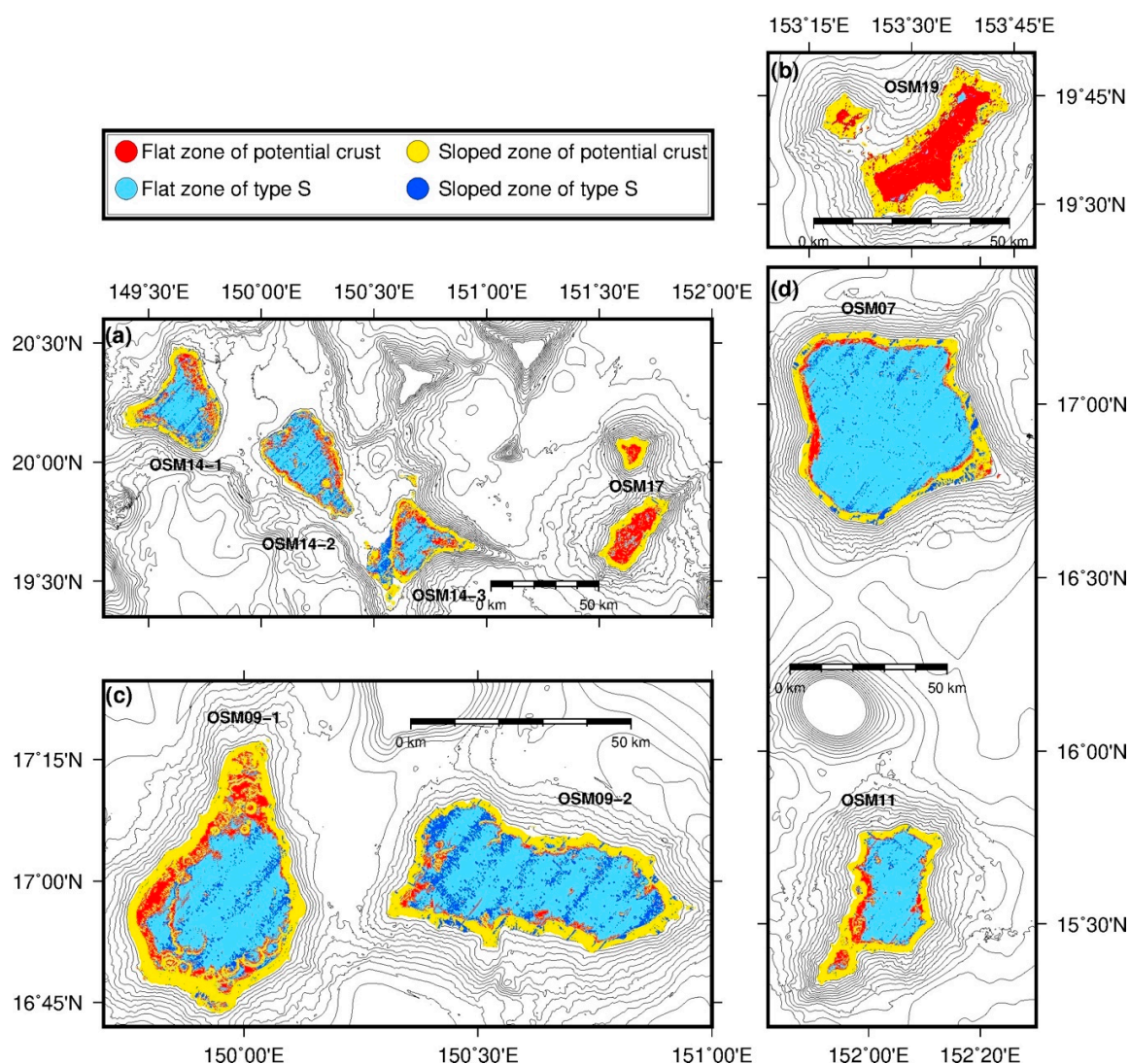


Figure 11. Spatial distribution map of Fe–Mn crust occurrences combining backscatter data, multibeam bathymetry, and ground-truth validation in the (a) northwest, (b) northeast, (c) southwest, and (d) south sectors of Figure 1b.

Table 1. Parameters used in mapping the spatial distribution of Fe–Mn crust occurrences in target’s regions with the exception of OSM 15, 16, and 18.

Seabed Type	Depth (m)	Slope Gradients (°)	Backscatter Intensity (dB)
Flat zone of type S			<−30
Flat zone of potential crust	>2500	<5	>−30
Sloped zone of type S			<−30
Sloped zone of potential crust		>5	>−30

Table 2. Accuracy of spatial distribution map of Fe–Mn crust occurrences.

Target	Potential Crust	Type S
Transect’s points correctly classified	2058	668
Transect’s points incorrectly classified	617	471
Total	2675	1139
Accuracy Rate	78%	59%

5. Conclusions

We conducted shipboard multibeam bathymetry and acoustic backscatter surveys across a series of seamounts in the Western Pacific Ocean to assess the spatial distribution of Fe–Mn crusts. A DCS was also operated within the multibeam survey area to estimate the relationship between MBES backscatter variations and the presence of Fe–Mn crusts. We focused on the periphery of the summit area of the seamounts where sedimentation varied owing to fluctuations in oceanographic conditions.

The shipboard MBES data, in combination with continuous video footage of the seabed, exhibited a positive correlation between high backscatter intensity, steep seabed slopes, and the occurrence of Fe–Mn crusts, but these observations were insufficient to discriminate the spatial boundaries between several seabed types that occurred over small areas, particularly in the transition zones or where discontinuous seabed types exist. We conclude that the existence of Fe–Mn crust deposits around sediment-dominated areas on the summit of the surveyed seamounts is a major factor influencing the bimodal distribution of acoustic backscatter intensities, with the exception of OSM 15, 16, and 18. Furthermore, variations above the minimum intermediate backscatter intensity (i.e., above -30 dB) primarily indicate seabed hardness variations reflecting the occurrence of substrates covered with Fe–Mn crusts.

Our results indicate that shipboard multibeam backscatter data are a valuable tool for assessing the potential of Fe–Mn crust deposits across a vast region. This approach also has significant implications for identifying the presence of Fe–Mn crust deposits around the outer rim of the summit area of a target seamount, which is more suitable for commercial mining operations.

Author Contributions: Conceptualization, J.K. and J.J.; methodology and analysis, S.-S.K., J.W.C., S.-J.P., J.K., and J.J.; resources, Y.K. and S.-K.S.; data curation, J.K. and J.J.; writing—original draft preparation, J.J.; writing—review and editing, J.K.; supervision, J.K.; project administration, J.K. and Y.K.; funding acquisition, S.-K.S. and J.-w.M. All authors have read and agreed to the published version of the manuscript.

Funding: This work was financially supported by funds from the Ministry of Oceans and Fisheries, Republic of Korea (19992001) and Korea Institute of Ocean Science and Technology (PE99824). S.-S.K. acknowledges support from the National Research Foundation of Korea (NRF) (MOE NRF-2017R1D1A1A02018632).

Acknowledgments: We thank scientists and crews of the R/V Onnuri for their support for the sampling and collecting data during the research cruises. We are grateful to reviewers for their constructive reviews.

Conflicts of Interest: The authors declare no conflict of interest.

References

1. Usui, A.; Okamoto, N. Geophysical and geological exploration of Cobalt-rich ferromanganese crusts: An attempt of small-scale mapping on a Micronesian seamount. *Mar. Georesour. Geotechnol.* **2010**, *28*, 192–206. [[CrossRef](#)]
2. Hein, J.R.; Mizell, K.; Koschinsky, A.; Conrad, T.A. Deep-ocean mineral deposits as a source of critical metals for high-and green-technology applications: Comparison with land-based resources. *Ore Geol. Rev.* **2013**, *51*, 1–14. [[CrossRef](#)]
3. Kim, J.; Ko, Y.; Hyeong, K.; Moon, J.W. Geophysical and geological exploration of cobalt-rich ferromanganese Crusts on a seamount in the Western Pacific. *Econ. Environ. Geol.* **2013**, *46*, 569–580. [[CrossRef](#)]
4. Scheirer, D.S.; Fornari, D.J.; Humphris, S.E.; Lerner, S. High-resolution seafloor mapping using the DSL-120 sonar system: Quantitative assessment of sidescan and phase-bathymetry data from the Lucky Strike segment of the Mid-Atlantic Ridge. *Mar. Geophys. Res.* **2000**, *21*, 121–142. [[CrossRef](#)]
5. Sen, A.; Ondreas, H.; Gaillot, A.; Marcon, Y.; Augustin, J.M.; Olu, K. The use of multibeam backscatter and bathymetry as a means of identifying faunal assemblages in a deep-sea cold seep. *Deep Sea Res. Part I* **2016**, *110*, 33–49. [[CrossRef](#)]
6. Siwabessy, P.J.W.; Tran, M.; Picard, K.; Brooke, B.P.; Huang, Z.; Smit, N.; Williams, D.K.; Nicholas, W.A.; Nichol, S.L.; Atkinson, I. Modelling the distribution of hard seabed using calibrated multibeam acoustic backscatter data in a tropical, macrotidal embayment: Darwin Harbour, Australia. *Mar. Geophys. Res.* **2018**, *39*, 249–269. [[CrossRef](#)]

7. Yoshikawa, S.; Okino, K.; Asada, M. Geomorphological variations at hydrothermal sites in the southern Mariana Trough: Relationship between hydrothermal activity and topographic characteristics. *Mar. Geol.* **2012**, *303*, 172–182. [[CrossRef](#)]
8. Thornton, B.; Asada, A.; Bodenmann, A.; Sangekar, M.; Ura, T. Instruments and methods for acoustic and visual survey of manganese crusts. *IEEE J. Ocean Eng.* **2013**, *38*, 186–203. [[CrossRef](#)]
9. Wilson, M.F.J.; O’Connell, B.; Brown, C.; Guinan, J.C.; Grehan, A.J. Multiscale terrain analysis of multibeam bathymetry data for habitat mapping on the continental slope. *Mar. Geod.* **2007**, *30*, 3–35. [[CrossRef](#)]
10. Brown, C.J.; Smith, S.J.; Lawton, P.; Anderson, J.T. Benthic habitat mapping: A review of progress towards improved understanding of the spatial ecology of the seafloor using acoustic techniques. *Estuar. Coast. Shelf Sci.* **2011**, *92*, 502–520. [[CrossRef](#)]
11. Parnum, I.M.; Gavrillov, A.N. High-frequency multibeam echo-sounder measurements of seafloor backscatter in shallow water: Part 1—Data acquisition and processing. *J. Underw. Technol.* **2011**, *30*, 3–12. [[CrossRef](#)]
12. Micallef, A.; Le Bas, T.P.; Huvenne, V.A.I.; Blondel, P.; Hühnerbach, V.; Deidun, A. A multi-method approach for benthic habitat mapping of shallow coastal areas with high-resolution multibeam data. *Cont. Shelf. Res.* **2012**, *39–40*, 14–26. [[CrossRef](#)]
13. De Moustier, C.P. Beyond bathymetry: Mapping acoustic backscattering from the deep seafloor with Sea Beam. *J. Acoust. Soc. Am.* **1986**, *79*, 316–331. [[CrossRef](#)]
14. Weydert, M. Measurement of Acoustic Backscattering of the Deep Seafloor Using a Deeply Towed Vehicle. A Technique to Investigate the Physical and Geological Properties of the Deep Seafloor and to Assess Manganese Nodule Resources. Ph.D. Thesis, University of California, San Diego, CA, USA, 1985.
15. Lee, S.H.; Kim, K.H. Side-scan sonar characteristics and manganese nodule abundance in the Clarion-Clipperton Fracture Zones NE equatorial Pacific. *Mar. Georesour. Geotechnol.* **2004**, *22*, 103–114. [[CrossRef](#)]
16. Ko, Y.; Lee, S.; Kim, J.; Kim, K.H.; Jung, M.S. Relationship between Mn nodule abundance and other geological factors in the northeastern Pacific: Application of GIS and probability method. *Ocean Sci. J.* **2006**, *41*, 149–161. [[CrossRef](#)]
17. Alevizos, E.; Schoening, T.; Koeser, K.; Snellen, M.; Greinert, J. Quantification of the fine-scale distribution of Mn-nodules: Insights from AUV multi-beam and optical imagery data fusion. *Biogeosci. Discuss.* **2018**, in review. [[CrossRef](#)]
18. Ferrini, V.L.; Flood, R.D. The effects of fine-scale surface roughness and grain size on 300 kHz multibeam backscatter intensity in sandy marine sedimentary environments. *Mar. Geol.* **2006**, *228*, 153–172. [[CrossRef](#)]
19. Sutherland, T.F.; Galloway, J.; Loschiavo, R.; Levings, C.D.; Hare, R. Calibration techniques and sampling resolution requirements for groundtruthing multibeam acoustic backscatter (EM3000) and QTC VIEW classification technology. *Estuar. Coast. Shelf Sci.* **2007**, *75*, 447–458. [[CrossRef](#)]
20. Jackson, D.R.; Winebrenner, D.P.; Ishimaru, A. Application of the composite roughness model to high-frequency bottom backscatter. *J. Acoust. Soc. Am.* **1986**, *79*, 1410–1422. [[CrossRef](#)]
21. Jackson, D.R.; Briggs, K.B.; Williams, K.L.; Richardson, M.D. Tests of models for high-frequency seafloor backscatter. *IEEE J. Ocean Eng.* **1996**, *21*, 458–470. [[CrossRef](#)]
22. de Moustier, C.P.; Alexandrou, D. Angular dependence of 12-kHz seafloor acoustic backscatter. *J. Acoust. Soc. Am.* **1991**, *90*, 522–531. [[CrossRef](#)]
23. APL. *APL-UW High-Frequency Ocean Environment Acoustic Models Handbook (APL-UW TR9407)*; Applied Physics Laboratory, University of Washington: Seattle, WA, USA, 1994; pp. 1–49.
24. Clarke, J.E. Towards remote seafloor classification using the angular response of acoustic backscattering: A case study from multiple overlapping GLORIA data. *IEEE J. Ocean Eng.* **1994**, *19*, 112–127. [[CrossRef](#)]
25. Talukdar, K.K.; Tyce, R.C.; Clay, C.S. Interpretation of Sea Beam backscatter data collected at the Laurentian fan off Nova Scotia using acoustic backscatter theory. *J. Acoust. Soc. Am.* **1995**, *97*, 1545–1558. [[CrossRef](#)]
26. Novarini, J.C.; Caruthers, J.W. A simplified approach to backscattering from a rough seafloor with sediment inhomogeneities. *IEEE J. Ocean Eng.* **1998**, *23*, 157–166. [[CrossRef](#)]
27. Williams, K.L.; Jackson, D.R.; Thorsos, E.I.; Tang, D.; Briggs, K.B. Acoustic backscattering experiments in a well characterized sand sediment: Data/model comparisons using sediment fluid and Biot models. *IEEE J. Ocean Eng.* **2002**, *27*, 376–387. [[CrossRef](#)]
28. Fonseca, L.; Mayer, L. Remote estimation of surficial seafloor properties through the application angular range analysis to multibeam sonar data. *Mar. Geophys. Res.* **2007**, *28*, 119–126. [[CrossRef](#)]

29. Parnum, I.M. Benthic Habitat Mapping Using Multibeam Sonar Systems. Ph.D. Thesis, Curtin University of Technology, Perth, Australia, 2007.
30. Gavrilov, A.N.; Parnum, I.M. Fluctuations of seafloor backscatter data from multibeam sonar systems. *IEEE J. Ocean Eng.* **2010**, *35*, 209–219. [[CrossRef](#)]
31. Hamilton, L.J.; Parnum, I.M. Acoustic seabed segmentation from direct statistical clustering of entire multibeam sonar backscatter curves. *Cont. Shelf Res.* **2011**, *31*, 138–148. [[CrossRef](#)]
32. Hasan, R.C.; Ierodiaconou, D.; Laurenson, L. Combining angular response classification and backscatter imagery segmentation for benthic biological habitat mapping. *Estuar. Coast. Shelf Sci.* **2012**, *97*, 1–9. [[CrossRef](#)]
33. Lurton, X.; Lamarche, G.; Brown, C.; Lucieer, V.L.; Rlce, G.; Schimel, A.; Weber, T. Backscatter Measurements by Seafloor-Mapping Sonars. Guidelines and Recommendations. *Collect. Rep. Memb. GeoHab Backscatter Work. Gr.* **2015**, *5*, 200.
34. Stewart, W.K.; Chu, D.; Malik, S.; Lerner, S.; Singh, H. Quantitative seafloor characterization using a bathymetric sidescan sonar. *IEEE J. Ocean Eng.* **1994**, *19*, 599–610. [[CrossRef](#)]
35. Richardson, M.D.; Briggs, K.B.; Williams, K.L.; Lyons, A.P.; Jackson, D.R. Effects of changing roughness on acoustic scattering: (2) anthropogenic changes. *Proc. Inst. Acoust.* **2001**, *23*, 343–390.
36. Briggs, K.B.; Tang, D.; Williams, K.L. Characterization of interface roughness of rippled sand off Fort Walton Beach, Florida. *IEEE J. Ocean Eng.* **2002**, *27*, 505–514. [[CrossRef](#)]
37. Joo, J.; Kim, J.; Ko, Y.; Kim, S.S.; Son, J.; Pak, S.J.; Ham, D.J.; Son, S.K. Characterizing geomorphological properties of western pacific seamounts for cobalt-rich ferromanganese crust resource assessment. *Econ. Environ. Geol.* **2016**, *49*, 121–134. [[CrossRef](#)]
38. Ryan, W.B.F.; Carbotte, S.M.; Coplan, J.O.; O'Hara, S.; Melkonian, A.; Arko, R.; Weissel, R.A.; Ferrini, V.; Goodwillie, A.; Nitsche, F.; et al. Global Multi-Resolution Topography synthesis. *Geochem. Geophys. Geosyst.* **2009**, *10*, Q03014. [[CrossRef](#)]
39. Caress, D.W.; Chayes, D.N. MB-System: Mapping the Seafloor. 2006. Available online: <http://www.mbari.org/data/mbsystem> (accessed on 6 January 2014).
40. Wessel, P.; Smith, W.H.F.; Scharroo, R.; Luis, J.F.; Wobbe, F. Generic mapping tools: Improved version released. *Eos Trans. AGU* **2013**, *94*, 409–410. [[CrossRef](#)]
41. Hellequin, L.; Lurton, X.; Augustin, J.M. Postprocessing and signal corrections for multibeam echosounder images. In Proceedings of the Oceans '97, MTS/IEEE Conference, Halifax, NS, Canada, 6–9 October 1997; pp. 23–26.
42. Hellequin, L.; Boucher, J.M.; Lurton, X. Processing of high-frequency multibeam echo sounder data for seafloor characterization. *IEEE J. Ocean Eng.* **2003**, *28*, 78–89. [[CrossRef](#)]
43. Le Gonidec, Y.; Lamarche, G.; Wright, I.C. Inhomogeneous Substrate Analysis Using EM300 Backscatter Imagery. *Mar. Geophys. Res.* **2003**, *24*, 311–327. [[CrossRef](#)]
44. Lamarche, G.; Lurton, X.; Verdier, A.L.; Augustin, J.M. Quantitative characterization of seafloor substrate and bedforms using advanced processing of multibeam backscatter—Application to the Cook Strait, New Zealand. *Cont. Shelf Res.* **2011**, *31*, S93–S109. [[CrossRef](#)]
45. Fonseca, L.; Calder, B. Geocoder: An efficient backscatter map constructor. In Proceedings of the U.S. Hydrographic Conference 2005, San Diego, CA, USA, 29–31 March 2005; pp. 1–9.
46. Blondel, P. *Handbook of Sidescan Sonar*; Springer: New York, NY, USA, 2009; pp. 15–18.
47. Lurton, X. *An Introduction to Underwater Acoustics: Principles and Applications*, 2nd ed.; Springer Praxis Publishing: London, UK, 2010; pp. 85–102.
48. Innangi, S.; Passaro, S.; Tonielli, R.; Mailano, G.; Ventura, G.; Tamburrino, S. Seafloor mapping using high-resolution multibeam backscatter: The Palinuro Seamount (Eastern Tyrrhenian Sea). *J. Maps* **2016**, *12*, 736–746. [[CrossRef](#)]
49. Urick, R.J. The backscattering of Sound from a Harbor Bottom. *J. Acoust. Soc. Am.* **1954**, *26*, 231–235. [[CrossRef](#)]
50. Williams, K.L.; Jackson, D.A.; Tang, D.; Briggs, K.B.; Thorsos, E.I. Acoustic backscattering from a sand and a sand/mud environment: Experiments and data/model comparisons. *IEEE J. Ocean Eng.* **2009**, *34*, 388–398. [[CrossRef](#)]
51. Yoo, C.H.; Joo, J.; Lee, S.H.; Ko, Y.; Chi, S.B.; Kim, H.J.; Seo, I.; Hyeong, K. Resource Assessment of Polymetallic Nodules Using Acoustic Backscatter Intensity Data from the Korean Exploration Area, Northeastern Equatorial Pacific. *Ocean Sci. J.* **2018**, *53*, 381–394. [[CrossRef](#)]

52. Clarke, J.E. Multispectral acoustic backscatter from multibeam, improved classification potential. In Proceedings of the U.S. Hydrographic Conference 2015, National Harbor, MD, USA, 16–19 March 2015; pp. 1–18.
53. Brown, C.J.; Beaudoin, J.; Brissette, M.; Gazzola, V. Setting the Stage for Multispectral Acoustic Backscatter Research. In Proceedings of the United States Hydrographic Conference, Galveston, TX, USA, 20–23 March 2017.
54. Gaida, T.C.; Ali, T.A.; Snellen, M.; Amiri-Simkooei, A.; Dijk, T.A.; Simons, D.G. A multispectral bayesian classification method for increased acoustic discrimination of seabed sediments using multi-frequency multibeam backscatter data. *Geosciences* **2018**, *8*, 455. [[CrossRef](#)]



© 2020 by the authors. Licensee MDPI, Basel, Switzerland. This article is an open access article distributed under the terms and conditions of the Creative Commons Attribution (CC BY) license (<http://creativecommons.org/licenses/by/4.0/>).